

Nonlinear one-way edge-mode interactions for frequency mixing in topological photonic crystals

Zhihao Lan, Jian Wei You, and Nicolae C. Panoiu*

Department of Electronic and Electrical Engineering, University College London,
Torrington Place, London, WC1E 7JE, United Kingdom

(Dated: March 24, 2022)

Topological photonics aims to utilize topological photonic bands and corresponding edge modes to implement robust light manipulation, which can be readily achieved in the linear regime of light-matter interaction. Importantly, unlike solid state physics, the common test bed for new ideas in topological physics, topological photonics provide an ideal platform to study wave mixing and other nonlinear interactions. These are well-known topics in classical nonlinear optics but largely unexplored in the context of topological photonics. Here, we investigate nonlinear interactions of one-way edge-modes in frequency mixing processes in topological photonic crystals. We present a detailed analysis of the band topology of two-dimensional photonic crystals with hexagonal symmetry and demonstrate that nonlinear optical processes, such as second- and third-harmonic generation can be conveniently implemented via one-way edge modes of this setup. Moreover, we demonstrate that more exotic phenomena, such as slow-light enhancement of nonlinear interactions and harmonic generation upon interaction of backward-propagating (left-handed) edge modes can also be realized. Our work opens up new avenues towards topology-protected frequency mixing processes in photonics.

One of the most important developments in condensed matter physics in the past decades is the discovery of topological insulating materials [1, 2]. These materials feature gapped bulk but gapless edge modes, which propagate unidirectionally along the system edge and are immune to local disorder, thus opening a promising avenue towards robust wave manipulation protected by topology. Inspired by this development, the emerging field of topological photonics aims to extend these topology related ideas to the realm of photonics [3–6], which holds great promises for innovative optical devices by exploiting robust, scattering-free light propagation and manipulation. As the concept of energy band exists at the single particle level both in condensed matter physics and photonics, the goal of realizing photonic topological insulators can be readily achieved in the linear regime of light matter interaction. Indeed, topological phenomena of electromagnetic waves in a linear medium can be understood by mapping Maxwell equations to the Schrödinger equation [7, 8].

Photonics, however, has several features not present in solid-state physics. For example, optical gain and loss can be utilized to implement non-Hermitian photonics based on parity-time symmetry [9]. The recently realized topological insulator laser demonstrates the power of this new ingredient and could deepen our understanding of the interplay between non-hermiticity and topology in active optical systems

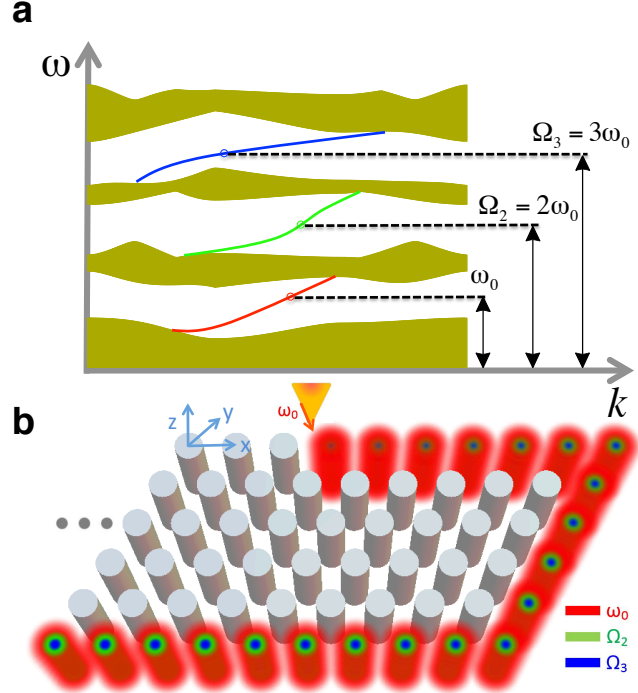


FIG. 1. **Nonlinear one-way edge mode interaction in 2D topological photonic crystals.** **a**, Schematic band structure showing the emergent edge modes due to the nontrivial topology of the bulk frequency bands. The edge modes can couple *via* SHG and THG frequency mixing processes. **b**, Real space illustration showing the unidirectional propagation of coupled edge modes along the system edge. The red arrow indicates the excitation source of the fundamental wave whereas the green and blue waves are generated as a result of nonlinear wave mixing.

[10, 11]. Another well-known feature is the existence of nonlinearity in many optical materials. In fact, optical nonlinear effects play a key rôle in modern photonic applications, giving rise to a variety of important phenomena, including the formation of solitons, modulation and all-optical switching of optical signals, and frequency conversion for the generation of ultrashort pulses [12]. Thus one expects new physics to emerge when adding nonlinearity to photonic systems with nontrivial topological properties. Indeed, it has been shown that when a photonic topological insulator is embedded in an optical medium with Kerr nonlinearity, lattice edge solitons could arise [13, 14]. The possibility to enhance the conversion efficiency of harmonic generation in the presence of topological edge states has also been studied [15, 16]. Moreover, traveling-wave amplifiers [17], topological sources of quan-

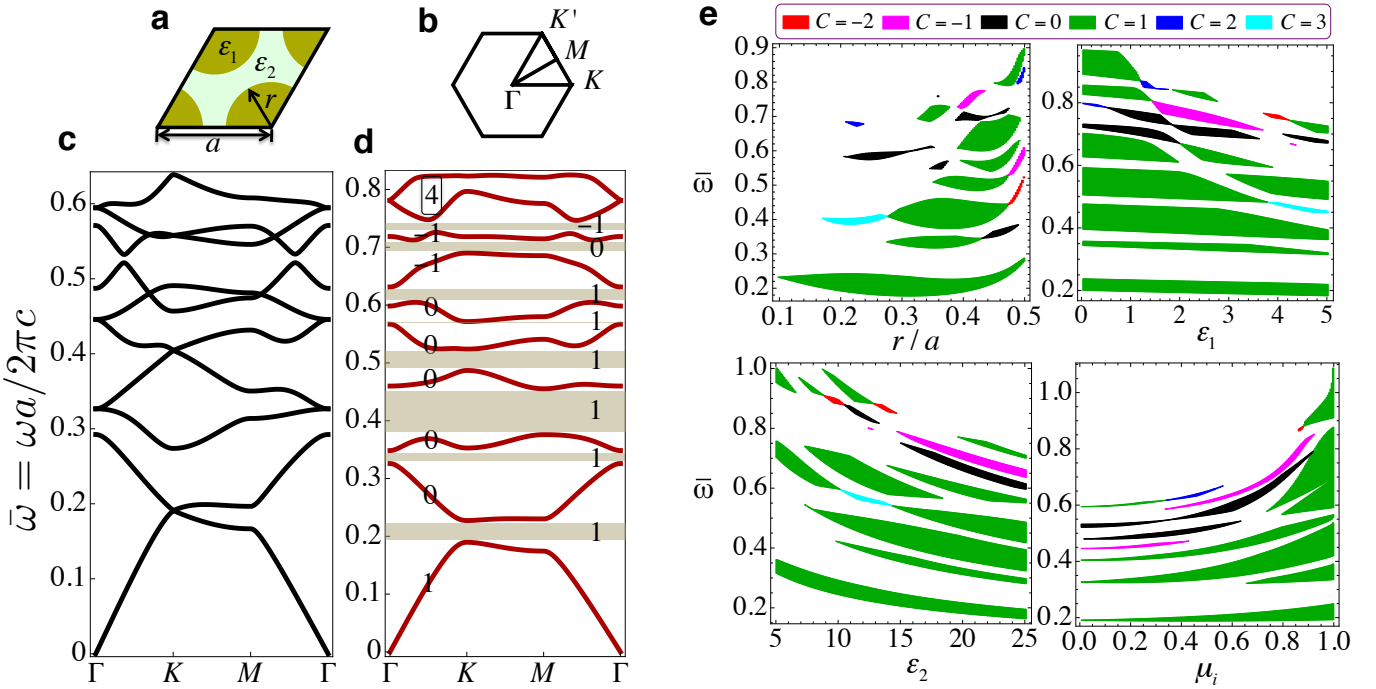


FIG. 2. **Topology of the bulk photonic bands and the Chern-number-graded gap phase diagrams.** **a**, The unit cell with lattice constant a of the PhC, where r and ϵ_1 are the radius and relative permittivity of the cylinders, respectively, and ϵ_2 and μ_i are the relative permittivity and off-diagonal component of the relative permeability of the background magnetic material, respectively. **b**, The first Brillouin zone with the symmetry points, Γ , K , K' , and M . **c**, Photonic band structure of the PhC, computed for $r = 0.4a$, $\epsilon_1 = 3$, $\epsilon_2 = 18$, and $\mu_i = 0$. **d**, Nontrivial topological bands for $\mu_i = 0.8$ (the other parameters are the same as in c), where the Chern number of each band and the gap Chern numbers are provided (except for the last two bands that touch each other and thus have the same Chern number). **e**, Chern-number-graded gap phase diagrams when varying r , ϵ_1 , ϵ_2 , and μ_i , determined for $r = 0.4a$, $\epsilon_1 = 3$, $\epsilon_2 = 18$, and $\mu_i = 0.8$.

tum light [18] and nonlinear mapping of photonic topological edge states [19] have also been achieved. Despite these important advances, the feasibility of achieving nonlinear optical mixing of edge states of topological photonic crystals, which is one of the most fundamental nonlinear optical processes, has not been explored yet.

In this work, we study nonlinear optical interactions of edge modes in topological photonic crystals (PhCs), as per Fig. 1. In particular, we present a detailed study of the band topology of two-dimensional (2D) photonic crystals with hexagonal symmetry by mapping out the Chern-number-graded gap phase diagrams. Interestingly, we find that most gaps of the phase diagrams have exactly one edge state in each gap, thus providing a convenient configuration to study the nonlinear interaction of these modes. To this end, by properly tailoring the edge configuration to achieve phase matching, we show that key nonlinear optical processes, such as second- and third-harmonic generation (SHG, THG) can be readily realized in this setup. Beyond this proof-of-principle demonstration of these nonlinear optical processes, we further show that some more exotic nonlinear optical phenomena can also be observed in these topological PhCs, including slow-light enhanced frequency conversion efficiency and higher-harmonic generation upon interaction of so-called backward-

propagating (left-handed) modes. All these novel ideas open up new avenues towards active photonic devices with novel functionalities for photonic applications.

RESULTS

The system. – We begin by describing the system setup. First, 2D PhCs possessing topological frequency gaps around frequencies of ω_0 , $\Omega_2 = 2\omega_0$, and $\Omega_3 = 3\omega_0$ are designed in order to study SHG and THG *via* the corresponding edge modes located inside these gaps. As such, in principle any PhC satisfying this condition could be employed. Nonetheless, it would be beneficial if the first gap is topological since typically, the spectral separation among frequency bands and the gap widths decrease as the frequency increases. In view of this, employing the transverse magnetic (TM) modes of a PhC with hexagonal symmetry lattice, which features Dirac cones at K and K' points of the first Brillouin zone (FBZ) between the first and second bands [20], is a natural choice. More specifically, one expects that for this configuration the first gap becomes topological when gapping the Dirac cones by breaking the time-reversal symmetry. Consequently, we consider triangular PhCs whose unit cell contains only one cylinder with radius, r , as depicted in Fig. 2a. Lattice structures with hexagonal symmetry but having more cylinders in each unit cell, like honeycomb and Kagome lattices with two and

three cylinders, respectively, could potentially be employed, too. The second step of our design procedure is to include magnetic and nonlinear materials. To guide potential experimental implementations and for the sake of specificity, we consider cylinders with low-permittivity (ϵ_1), non-magnetic nonlinear material immersed in a magnetic background material with high-permittivity (ϵ_2). Note that the permittivity of the cylinders has to be lower than that of the background to ensure that Dirac cones exist.

Topological properties of the bulk frequency bands. – We now move on to the topological properties of the bulk frequency bands of the proposed non-magnetic ($\mu = \mu_0$) PhCs whose unit cell and FBZ are shown in Figs. 2a and 2b. In the following, we use normalized frequency and momentum, $\bar{\omega} = \omega a / 2\pi c$ and $\bar{k} = ka/\pi$, respectively, where c is the speed of light and a is the lattice constant. Figure 2c shows the photonic band structure of the PhC with $r = 0.4a$, $\epsilon_1 = 3$, and $\epsilon_2 = 18$ from which one can see the Dirac cone between the first and second bands at K and K' points.

As known, the Chern number of each band is zero in systems with time-reversal symmetry [21]. A common way to break time-reversal symmetry and generate bands with nonzero Chern number is to use magnetic materials [22–25], where the permeability tensor of the material under an external magnetic field along the z -axis possesses off-diagonal components in the $x - y$ plane, *i.e.*,

$$\mu = \begin{pmatrix} \mu_0 & i\mu_i & 0 \\ -i\mu_i & \mu_0 & 0 \\ 0 & 0 & \mu_0 \end{pmatrix}. \quad (1)$$

Here, we set $\mu_0 = 1$ and take μ_i as a parameter to quantify the effect of time-reversal symmetry breaking. Figure 2d shows the photonic band structure for $\mu_i = 0.8$, where one can see that the Dirac cone is now gapped.

To characterize the topology of the frequency bands, we calculate the Chern number of the n th band, defined as [3, 7]:

$$C_n = \frac{1}{2\pi} \iint_{FBZ} \mathcal{F}_n(\mathbf{k}) \cdot d\mathbf{k}, \quad (2)$$

where $\mathcal{A}_n(\mathbf{k}) = \langle \mathbf{E}_n(\mathbf{k}) | i\nabla_{\mathbf{k}} | \mathbf{E}_n(\mathbf{k}) \rangle$ and $\mathcal{F}_n(\mathbf{k}) = \nabla_{\mathbf{k}} \times \mathcal{A}_n(\mathbf{k})$ are the Berry connection and Berry curvature, respectively, with $\mathbf{E}_n(\mathbf{k})$ being the electric field of the n th band mode with momentum, \mathbf{k} . The momentum-space integral is performed over the FBZ, whereas the inner product of the Berry connection is defined as $\langle \mathbf{E}_\alpha | \mathbf{E}_\beta \rangle = \iint \epsilon(\mathbf{r}) \mathbf{E}_\alpha(\mathbf{r}) \cdot \mathbf{E}_\beta(\mathbf{r}) d\mathbf{r}$, with the real-space integral performed over the unit cell. The Chern number is calculated using the algorithm described in [26] (for details, see Methods).

The calculated Chern numbers of the photonic bands are indicated in Fig. 2d on top of each band, and the gap Chern number, defined as the sum of the Chern numbers of the bands below the gap, is also given for each gap. The gap Chern number characterizes the topology of the gap in the sense that its sign determines the propagation direction of the edge modes and its value indicates the number of edge states located inside

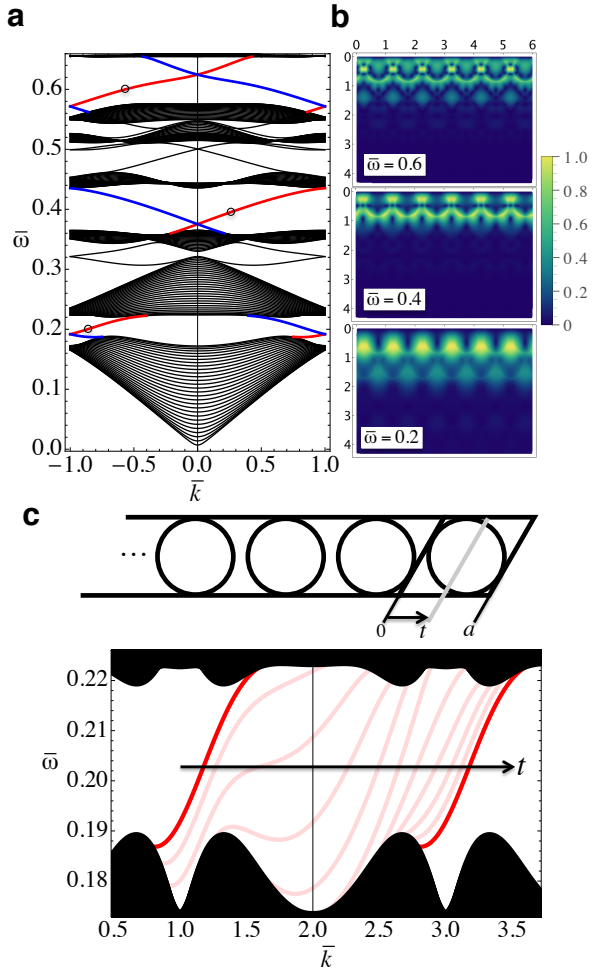


FIG. 3. Emergent edge modes due to the nontrivial topology of the bulk frequency bands. **a**, Photonic band structure of a 1D PhC strip that is periodic along the x -axis and has finite size of 30 unit cells along the y -axis (top and bottom edges are terminated by a perfect electric conductor at $r = 0.42a$). The other simulation parameters are $\epsilon_1 = 3$, $\epsilon_2 = 20$, and $\mu_i = 0.8$. The edge modes in the three gaps around $\bar{\omega} = 0.2, 0.4$, and 0.6 are depicted by red and blue lines and are formed at the top and bottom edges of the PhC, respectively. **b**, Field profiles of the three one-way edge modes at $\bar{\omega} = 0.2, 0.4$, and 0.6 of the top edge. Exponential decay of the field around the PhC edge can be observed (integers indicate the number of unit cells). **c**, Dispersion curves of edge modes can be tailored by changing the edge termination, as indicated in the sketch.

the gap [3]. An interesting feature revealed by Fig. 2d is that the first few gaps have Chern number $C = 1$, which means that there is one edge mode in each gap and all propagate in the same direction. Therefore, this configuration provides a convenient platform to study nonlinear optical processes, *e.g.*, SHG and THG.

To understand intuitively what regimes can be achieved with this setup, it is instructive to map out the Chern-number-graded gap phase diagrams, defined as the variation of the gap Chern numbers with the system parameters r , ϵ_1 , ϵ_2 , and μ_i . We show these gap phase diagrams in Fig. 2e for $r = 0.4a$,

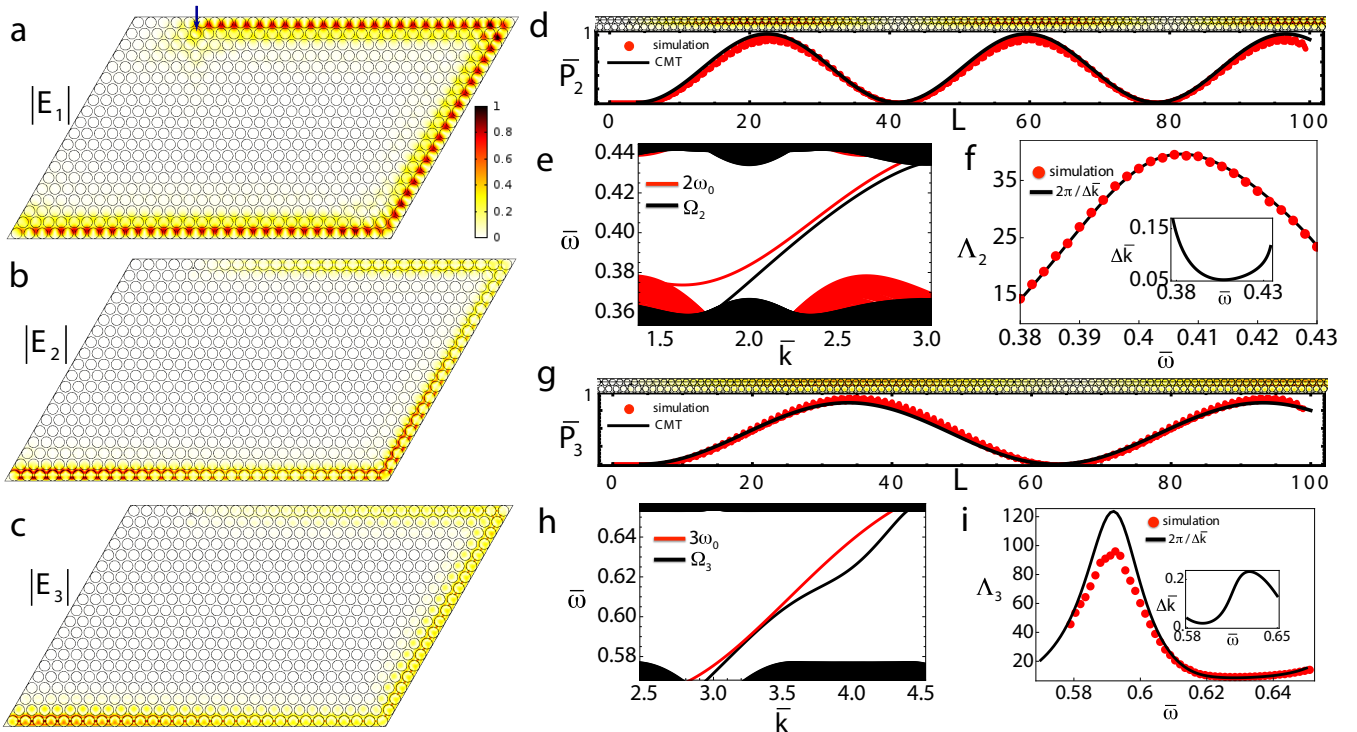


FIG. 4. SHG and THG *via* interaction of topological edge modes. **a, b, c**, Simulated field profile intensities of \mathbf{E}_1 , \mathbf{E}_2 , and \mathbf{E}_3 at $\bar{\omega} = 0.2$, $\bar{\Omega}_2 = 2\bar{\omega} = 0.4$, and $\bar{\Omega}_3 = 3\bar{\omega} = 0.6$, respectively, where \mathbf{E}_1 is induced by an external source indicated by an arrow, whereas \mathbf{E}_2 and \mathbf{E}_3 are generated by the corresponding nonlinear polarizations. The SHG and THG are simulated separately with $\chi^{(2)} = 10^{-21} \text{ CV}^{-2}$ and $\chi^{(3)} = 10^{-30} \text{ C m V}^{-3}$. In the simulations, absorbing boundary condition (ABC) is used for the left edge and PEC for the other edges. **d, e, f**, Detailed analysis of SHG, where **d** shows the field intensity profile and power \bar{P}_2 (normalized by its peak value) at SH in a much larger simulation domain so as to resolve the oscillations of \bar{P}_2 due to a small phase mismatch $\Delta\bar{k}$ of the edge modes at FF $\bar{\omega} = 0.2$ and SH $\bar{\Omega}_2 = 0.4$ (dotted and solid lines correspond to full numerical simulations and CMT, respectively); **e** shows the edge modes at FF ω_0 (plotted in terms of $2\omega_0$) and for the SHG, Ω_2 ; **f** shows the effect of phase matching, where the theoretically calculated $\Lambda_2 = 2\pi/\Delta\bar{k}$ and numerically extracted oscillation period of \mathbf{E}_2 are in excellent agreement. The $\bar{\omega}(\Delta\bar{k})$ curve is calculated according to the edge modes presented in **e**. **g, h, i**, The results corresponding to **d, e, f**, respectively, but calculated for the THG.

$\epsilon_1 = 3$, $\epsilon_2 = 18$, and $\mu_i = 0.8$, when one parameter is varied while keeping fixed the others. The results show that most domains of the phase diagrams have $C = 1$. Moreover, one can also see gaps with $C = 2$, $C = 3$ and, importantly, even gaps with negative Chern numbers, $C = -1$ and $C = -2$. As we will demonstrate, this variety of values of the gap Chern numbers leads to particularly rich physics when nonlinear interactions of topological modes are considered.

Topological properties of the edge states. – Guided by the phase diagrams in Fig. 3e, we choose the suitable parameters to create photonic gaps suitable to study SHG and THG. According to the principle of bulk-edge correspondence in systems with finite size, when the gap has nonzero Chern number, one-way edge modes will emerge in the gap. We present in Fig. 3a the photonic band structure of a PhC strip with 30 unit cells along the y -axis and periodic along the x -axis. This figure illustrates the emergence of various edge states across bulk photonic gaps in a range of frequencies. For the sake of clarity, we mark in red and blue the edge states formed on the top and bottom edges of the PhC strip, respectively. The field profiles of the edge states at frequencies $\bar{\omega} = 0.2$, $\bar{\Omega}_2 = 2\bar{\omega} = 0.4$,

and $\bar{\Omega}_3 = 3\bar{\omega} = 0.6$, presented in Fig. 3b, highlight the key feature of the edge state – exponential decay of the field away from the edge.

A well-known prerequisite for achieving efficient frequency conversion processes is to phase match the interacting waves [12]. In the current context, this requires a method to tune the wave vectors of the edge modes. As far as we know this issue has not been previously discussed, perhaps due to the irrelevance of phase matching in other (linear) physics involving edge modes. We find that the wave vector of edge modes can be readily tuned by simply changing the configuration of the edge termination. Figure 3c shows how the edge-mode band of the top edge changes when varying the location of the edge termination (see the sketch at the top of Fig. 3c). In general, we find that the edge-mode band shifts by about one reciprocal lattice vector, $G = 2\pi/a$, as one increases the width of the PhC strip by one unit cell. Note that due to the periodicity of the system along the x -axis, one can always shift the wave vector of the edge mode to the region of $[-\pi/a, \pi/a]$ by adding a momentum of nG , with n a suitable integer.

SHG and THG upon edge-mode interaction. – After a

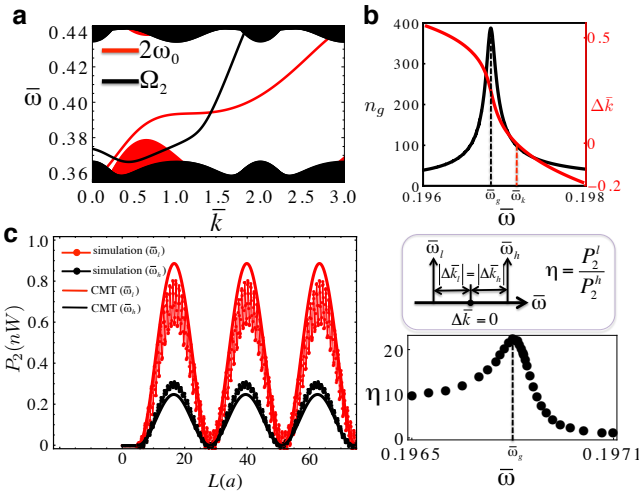


FIG. 5. The slow-light regime of SHG. **a**, Dispersion of edge modes at ω_0 and Ω_2 determined for $t = 0.24a$, as in Fig. 3c, whereas the other simulation parameters are the same as those in Fig. 4. **b**, The dispersion curve of the FF mode now shows a plateau leading to a peak of n_g at $\bar{\omega}_g = 0.1968$. The frequency of the phase-matching point $\bar{\omega}_k \equiv \bar{\omega}(\Delta\bar{k} = 0)$ is $\bar{\omega}_k = 0.1972$. **c**, The enhancement of the SH conversion efficiency due to the slow-light effect. The left panel shows an example where the SH power P_2 at two different frequencies, $\bar{\omega}_l = 0.1960$ and $\bar{\omega}_h = 0.1975$, shows the same oscillation period, yet its oscillation amplitude at $\bar{\omega}_l$ (closer to the maximum of n_g , located at $\bar{\omega}_g$) is enhanced compared to that at $\bar{\omega}_h$. The right panels show schematically the formal definition of the enhancement factor η (top) and its frequency dependence in the slow-light regime (bottom).

general discussion of the topological properties of the bulk photonic bands and edge modes, we now investigate nonlinear frequency conversion processes *via* the edge modes indicated in Fig. 3a using full-wave numerical simulations of Maxwell equations, with the results being summarized in Fig. 4. In the following, we mainly focus on the discussion of SHG, as the results of THG can be understood similarly.

We consider cylinders made of homogeneous and isotropic nonlinear material with a scalar nonlinear second-order susceptibility of $\chi^{(2)} = 10^{-21} \text{ C V}^{-2}$ (typical value of $\chi^{(2)}$ varies from $10^{-24} \text{ C V}^{-2}$ to $10^{-21} \text{ C V}^{-2}$ [27]). The pump electric field \mathbf{E}_1 is induced by an external source whereas \mathbf{E}_2 by the nonlinear polarization at the SH, generated by \mathbf{E}_1 . The amplitude of \mathbf{E}_1 is chosen such that the undepleted pump approximation holds, *i.e.* the amplitude of \mathbf{E}_1 is much larger than that of \mathbf{E}_2 and thus \mathbf{E}_1 is roughly constant during the frequency conversion process. Note, however, that our analysis remains valid when this condition is not fulfilled, too, our choice being chiefly guided by a more facile comparison between numerical and theoretical results, which is possible in this propagation regime.

From Figs. 4a and 4b, one can observe that the field profiles of \mathbf{E}_1 and \mathbf{E}_2 are indeed the same as the profiles of the edge modes shown in Fig. 3b, indicating that the two edge modes are indeed nonlinearly interacting *via* the SHG – a key result

of our work. The physics of this nonlinear process can be accurately captured by the coupled-mode theory (CMT) (see Methods and Supplementary Material). In particular, the period of spatial oscillations of the SH field \mathbf{E}_2 is determined by the wave-vector mismatch $\Delta k = k_{SH} - 3k_{FF}$ ($\Delta k = k_{TH} - 3k_{FF}$ for THG). As a result, we can straightforwardly compare the numerically extracted oscillation period of \mathbf{E}_2 with the theoretical prediction of $\Lambda_2 = 2\pi/\Delta k$, thus confirming that the key physics of nonlinear frequency conversion processes is validated by our simulations.

We further validate these conclusions using a much larger simulation domain, with the corresponding results being presented in Figs. 4d–4f. In Fig. 4d, where $\bar{\omega}_0 = 0.2$, $\bar{\Omega}_2 = 0.4$, and $\Delta\bar{k} = 0.054$, we have $\Lambda_2 = 37$. The agreement between the predictions the CMT and direct numerical simulations, of both the period and amplitude of SH power oscillation along the propagation distance, is excellent. We calculate $\Delta\bar{k}$ for all the frequencies of the interacting edge modes from Fig. 4e and present the theoretically calculated and numerically extracted oscillation period Λ_2 in Fig. 4f. An excellent agreement between the two results can be observed, which confirms the key physics of SHG, namely phase matching is indeed at work in our photonic system and SHG purely *via* nonlinear interaction of edge modes occurs in our setup. We also confirm the edge mode mediated THG as shown in Figs. 4g–4i, where the discrepancy in Fig. 4i between the numerical and theoretical results is due to inherent limitations of numerical simulations at very small Δk .

SHG in the slow-light regime. – The slow-light regime, characterized by a significantly reduced group velocity, $v_g = d\omega/dk$, can be particularly effective in enhancing the efficiency of nonlinear wave interactions. In the context of SHG, this can be achieved when v_g is reduced at one or both interacting waves. As Fig. 3c suggests, when one varies the location of the edge termination, the shift of the dispersion curve of the edge modes is accompanied by a change of its shape. For example, we find that for $t = 0.24a$, the dispersion curve of the edge mode at the FF has a plateau (see Fig. 5a) leading to a peak of the group index, $n_g = c/v_g$, at $\bar{\omega}_g$ (see Fig. 5b, where we define the slow-light regime by the condition $n_g > 20$ [28]). On the other hand, the fact that the phase-matching spectral point $\bar{\omega}_k \equiv \bar{\omega}(\Delta\bar{k} = 0) \neq \bar{\omega}_g$ provides a valuable approach to study the interplay between slow-light and phase-matching effects in the enhancement of SH conversion efficiency.

To this end, we fix the power of FF at $P_1 = 1 \text{ W}$ and compare the conversion efficiencies at two frequencies $\bar{\omega}_l$ and $\bar{\omega}_h$, lower and higher as compared to $\bar{\omega}_k$, respectively, chosen such that $\Delta\bar{k}(\bar{\omega}_l) = -\Delta\bar{k}(\bar{\omega}_h)$ (see the sketch in Fig. 5c). As such, phase-matching has the same influence on the wave interaction in the two cases and the conversion efficiency enhancement, $\eta = P_2(\bar{\omega}_l)/P_2(\bar{\omega}_h)$, is purely due to slow-light effects. The results in Fig. 5c show that slow-light contribution to η can be larger than 20×. Alternative scenarios to enhance the SH conversion efficiency can also be devised, *e.g.*, by using PhCs for which $\bar{\omega}_k = \bar{\omega}_g$ or PhCs for which the edge modes at

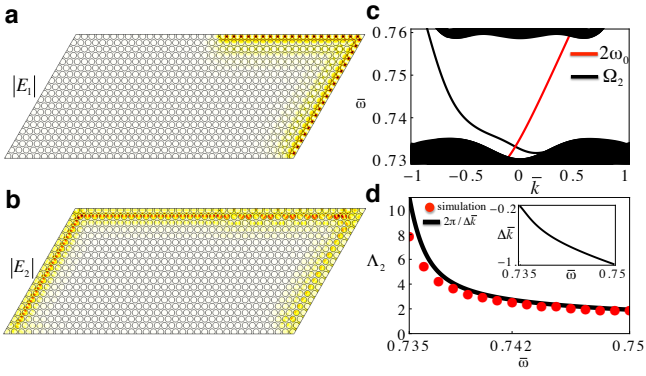


FIG. 6. SHG via interaction between forward- and backward-propagating edge modes. This setting exploits the existence of a gap with negative Chern number at the SH for $r = 0.41a$, $\epsilon_1 = 3$, $\epsilon_2 = 20$, $\mu_i = 0.82$ (see Fig. 2e) and edge termination at $t = 0.82a$ (see Fig. 3c). **a, b**, Field intensity profiles of E_1 and E_2 calculated for $2\omega_0 = 0.74$, illustrating that whereas the mode at the FF propagates clockwise ($C = 1$ for the ω_0 gap), the edge mode at the SH is backward-propagating ($C = -1$ for the Ω_2 gap). In the simulation, ABC is used for the bottom edge while PEC boundaries for the other edges. **c**, Edge states of the two gaps, which show the hallmark of edge modes with negative Chern number: the slope of the dispersion curve of the edge mode at the SH is negative. **d**, Comparison between the theoretically calculated and the numerically extracted oscillation period Λ_2 , confirming that the phase matching mechanism is involved in this unusual nonlinear interaction regime.

both the FF and SH are slow-light edge modes.

SHG via interaction between forward- and backward-propagating edge modes. – We now move on to an important class of nonlinear processes, which are challenging to achieve in regular optical media, and demonstrate SHG *via* interaction of backward-propagating edge modes. To this end, we exploit the existence of photonic gaps with negative Chern number in our system, as per Fig. 2e. In particular, we explore a case where the gap at the FF has $C = 1$, while the gap at the SH has $C = -1$. The corresponding edge modes are shown in Fig. 6c, which illustrates the signature of modes with negative Chern number, *i.e.*, the slope of the mode dispersion curve (at Ω_2) is negative. The simulation results of the field profiles are presented in Figs. 6a and 6b. It clearly shows that whereas the mode at the FF propagates clockwise, as it is a forward-propagating mode, the SH wave propagates counterclockwise because in the left-half region of the simulation domain there is no field at the FF and consequently no nonlinear polarization at the SH (note that we placed the source of the FF wave at the middle of the top edge and used absorbing boundary condition for the bottom edge). We also confirm that the phase matching mechanism is involved in this unusual mode interaction regime, as per the results in Fig. 6d. This backward-propagating mode regime is promising for practical applications where one requires to separate the FF mode from the mode generated at the SH.

Experimental considerations. – Since we separate the magnetic and nonlinear material components as the back-

ground and cylindrical regions of the PhC, respectively, possible experimental implementations could be readily conceived. For example, to demonstrate the topology-protected SHG, one can use as the background medium yttrium iron garnet (YIG) [29], a magnetic material widely used in recent experiments in topological photonics [22–25]. This material has relative permittivity $\epsilon = 15$ and saturation magnetization of $4\pi M_s = 1780$ Gauss. At frequency of 10 GHz and an external magnetic field of $H_0 = 1000$ Oe along the z -axis, the components of the permeability of YIG in the $x - y$ plane are $\mu_{\text{diag}} = 0.85$ and $\mu_{\text{off-diag}} = 0.54$. For the nonlinear material, one could use NaNO_2 , which has relative permittivity of $\epsilon = 4.18$ and $\chi^{(2)} = 3.2 \times 10^{-22} \text{ C V}^{-2}$ at frequency of tens of GHz [30]. Setting the radius of the cylinders to $r = 0.35a$, with $a \approx 3$ mm, the system has topological band gaps at $\bar{\omega}_0 \in [0.195, 0.23]$ and $\bar{\Omega}_2 \in [0.385, 0.41]$, so that SHG is achieved in the frequency interval of $\bar{\omega}_0 \in [0.195, 0.205]$. The effects of material losses and frequency dispersion in a ferrite at microwave frequencies have been discussed in Ref. [21], showing that for YIG, the decay length is around $1300a$, thus far exceeding practical structural dimensions, and the band gap width slightly decreases by about 6%.

Discussion. – In this work, we have demonstrated topology-protected nonlinear frequency conversion processes via one-way edge modes of topological photonic crystals. Apart from the proof-of-concept implementations, such as SHG and THG, we also showed that more complex behaviors, such as slow-light effects and counter-propagating mode interaction, can also be realized within the setup. A special aspect of nonlinear processes, *i.e.*, the phase-matching condition, requires a new level of control of the edge modes, which has not been discussed previously. This condition requires a method to tune the dispersion of the edge modes, which we found can be conveniently achieved by tailoring the geometry of the edge termination. Our proposed setup provides a platform for studying additional phenomena, *e.g.*, when the frequency gap has large Chern number ($|C| \neq 0, 1$ [31]) one can explore how to excite one of the several edge modes in the gap or how to couple edge modes belonging to different gaps via the nonlinearity of the medium.

Importantly, nonlinear interactions of topological modes, such as sum- and difference-frequency generation, high-harmonic generation, and four-wave-mixing, can be readily implemented within our setup. Our work may also stimulate the search for other lattice geometries or setups where one can optimize the gap properties for specific applications. Thus, in the Chern number graded gap phase diagrams of Fig. 2e, apart from the gap of $C = 1$, other gaps with $C = -1, -2, 2, 3$ are typically narrow and appear at high frequencies, so designing setups where these gaps are wide and are formed at low frequencies is particularly relevant from experimental point of view. Last but not least, the concept of topology-protected nonlinear frequency mixing is universal in that it applies not only to photonics, but also to plasmonics [32–35], phononics [36–38], magnonics [39–41], and metamaterials [42, 43], thus we expect that our work will generate a broad impact.

* n.panoiu@ucl.ac.uk

[1] Hasan, M. Z. and Kane, C. L. Colloquium: Topological insulators. *Rev. Mod. Phys.* **82**, 3045 (2010).

[2] Qi, X.-L. and Zhang, S.-C. Topological insulators and superconductors. *Rev. Mod. Phys.* **83**, 1057 (2011).

[3] Lu, L., Joannopoulos, J. D. and Soljacic, M. Topological photonics. *Nat. Photonics* **8**, 821-829 (2014).

[4] Khanikaev, A. B. and Shvets, G. Two-dimensional topological photonics. *Nat. Photonics* **11**, 763-773 (2017).

[5] Ozawa, T., Price, H. M., Amo, A., Goldman, N., Hafezi, M., Lu, L., Rechtsman, M., Schuster, D., Simon, J., Zilberman, O., and Carusotto, I. Topological Photonics. *Rev. Mod. Phys.* **91**, 015006 (2019).

[6] Xie, B.-Y., Wang, H.-F., Zhu, X.-Y., Lu, M.-H., Wang, Z. D., and Chen, Y.-F. Photonics meets topology. *Opt. Express* **26**, 24531-24550 (2018).

[7] Haldane, F. D. M. and Raghu, S. Possible Realization of Directional Optical Waveguides in Photonic Crystals with Broken Time-Reversal Symmetry. *Phys. Rev. Lett.* **100**, 013904 (2008).

[8] Nittis, G. D. and Lein, M. On the role of symmetries in the theory of photonic crystals. *Ann. Phys.* **350**, 568-587 (2014).

[9] Feng, L., El-Ganainy, R. and Ge, L. Non-Hermitian photonics based on parity-time symmetry. *Nat. Photonics* **11**, 752-762 (2017).

[10] Harari, G., Bandres, M. A., Lumer, Y., Rechtsman, M. C., Chong, Y. D., Khajavikhan, M., Christodoulides, D. N. and Segev, M. Topological insulator laser: Theory. *Science* **359**, eaar4003 (2018).

[11] Bandres, M. A., Wittek, S., Harari, G., Parto, M., Ren, J., Segev, M., Christodoulides, D. N. and Khajavikhan, M. Topological insulator laser: Experiments. *Science* **359**, eaar4005 (2018).

[12] Boyd, R. W. *Nonlinear Optics* (Academic Press; 3 edition 2008).

[13] Lumer, Y., Plotnik, Y., Rechtsman, M. C. and Segev, M. Self-Localized States in Photonic Topological Insulators. *Phys. Rev. Lett.* **111**, 243905 (2013).

[14] Leykam, D. and Chong, Y. D. Edge Solitons in Nonlinear-Photonic Topological Insulators. *Phys. Rev. Lett.* **117**, 143901 (2016).

[15] Qian, C., Choi, K. H., Wu, R. P. H., Zhang, Y., Guo, K. and Fung, K. H. Nonlinear frequency up-conversion via double topological edge modes. *Opt. Express* **26**, 5083-5091 (2018).

[16] Wang, Y., Lang, L.-J., Lee, C. H., Zhang, B. and Chong, Y. D. Topologically enhanced harmonic generation in a nonlinear transmission line metamaterial. *Nat. Commun.* **10**, 1102 (2019).

[17] Peano, V., Houde, M., Marquardt, F., and Clerk, A. A. Topological Quantum Fluctuations and Traveling Wave Amplifiers. *Phys. Rev. X* **6**, 041026 (2016).

[18] Mittal, S., Goldschmidt, E. A. and Hafezi, M. A topological source of quantum light. *Nature* **561**, 502-506 (2018).

[19] Smirnova, D., Kruk, S., Leykam, D., Melik-Gaykazyan, E., Choi, D.-Y., and Kivshar, Y. Nonlinear mapping of photonic topological edge states. Preprint at <https://arxiv.org/abs/1811.12130> (2018).

[20] Joannopoulos, J. D., Johnson, S. G., Winn, J. N. and Meade, R. D. *Photonic Crystals: Molding the Flow of Light*. (Princeton University Press; Second edition 2008).

[21] Wang, Z., Chong, Y. D., Joannopoulos, J. D. and Soljacic, M. Reflection-Free One-Way Edge Modes in a Gyromagnetic Photonic Crystal. *Phys. Rev. Lett.* **100**, 013905 (2008).

[22] Wang, Z., Chong, Y., Joannopoulos, J. D. and Soljacic, M. Observation of unidirectional backscattering-immune topological electromagnetic states. *Nature* **461**, 772-775 (2009).

[23] Skirlo, S. A., Lu, L., Igarashi, Y., Yan, Q., Joannopoulos, J. and Soljacic, M. Experimental Observation of Large Chern Numbers in Photonic Crystals. *Phys. Rev. Lett.* **115**, 253901 (2015).

[24] Bahari, B., Ndao, A., Vallini, F., Amili, A. E., Fainman, Y. and Kante, B. Nonreciprocal lasing in topological cavities of arbitrary geometries. *Science* **358**, 636-640 (2017).

[25] Li, F.-F., Wang, H.-X., Xiong, Z., Lou, Q., Chen, P., Wu, R.-X., Poo, Y., Jiang, J.-H. and John, S. Topological light-trapping on a dislocation. *Nat. Commun.* **9**, 2462 (2018).

[26] Fukui, T., Hatsugai, Y., and Suzuki, H. Chern Numbers in Discretized Brillouin Zone: Efficient Method of Computing (Spin) Hall Conductances. *J. Phys. Soc. Jpn.* **74**, 1674-1677 (2005).

[27] Saleh, B. E. A. and Teich, M. C. *Fundamentals of Photonics* (Wiley Series in Pure and Applied Optics). (Wiley-Blackwell; 2Rev Ed edition 2007).

[28] Lavdas, S. and Panoiu, N. C. Theory of pulsed four-wave mixing in one-dimensional silicon photonic crystal slab waveguides. *Phys. Rev. B* **93**, 115435 (2016).

[29] Pozar, D. M. *Microwave Engineering*. (John Wiley & Sons; 4th edition 2011).

[30] Boyd, G. D., Bridges, T. J., Pollack, M. A., and Turner, E. H. Microwave Nonlinear Susceptibilities Due to Electronic and Ionic Anharmonicities in Acentric Crystals. *Phys. Rev. Lett.* **26**, 387 (1971).

[31] Skirlo, S. A., Lu, L. and Soljacic, M. Multimode One-Way Waveguides of Large Chern Numbers. *Phys. Rev. Lett.* **113**, 113904 (2014).

[32] Jin, D., Christensen, T., Soljacic, M., Fang, N. X., Lu, L. and Zhang, X. Infrared Topological Plasmons in Graphene. *Phys. Rev. Lett.* **118**, 245301 (2017).

[33] Pan, D., Yu, R., Xu, H. and de Abajo, F. J. G. Topologically protected Dirac plasmons in a graphene superlattice. *Nat. Commun.* **8**, 1243 (2017).

[34] Kauranen, M. and Zayats, A. V. Nonlinear plasmonics. *Nat. Photonics* **6**, 737-748 (2012).

[35] Panoiu, N. C., Sha, W., Lei, D. Y. and Li, G. C. Nonlinear optics in plasmonic nanostructures. *J. Opt.* **20**, 083001 (2018).

[36] Yang, Z., Gao, F., Shi, X., Lin, X., Gao, Z., Chong, Y. and Zhang, B. Topological Acoustics. *Phys. Rev. Lett.* **114**, 114301 (2015).

[37] Bojahr, A., Gohlke, M., Leitenberger, W., Pudell, J., Reinhardt, M., von Reppert, A., Roessle, M., Sander, M., Gaal, P. and Bargheer, M. Second Harmonic Generation of Nanoscale Phonon Wave Packets. *Phys. Rev. Lett.* **115**, 195502 (2015).

[38] Ge, H., Yang, M., Ma, C., Lu, M.-H., Chen, Y.-F., Fang, N. and Sheng, P. Breaking the barriers: advances in acoustic functional materials. *Natl. Sci. Rev.* **5**, 159-182 (2018).

[39] Chumak, A. V., Vasyuchka, V. I., Serga, A. A. and Hillebrands, B. Magnon spintronics. *Nat. Phys.* **11**, 453-461 (2015).

[40] Sebastian, T., Bracher, T., Pirro, P., Serga, A. A., Hillebrands, B., Kubota, T., Naganuma, H., Oogane, M. and Ando, Y. Nonlinear Emission of Spin-Wave Caustics from an Edge Mode of a Microstructured Co₂Mn_{0.6}Fe_{0.4}Si Waveguide. *Phys. Rev. Lett.* **110**, 067201 (2013).

[41] Wang, X. S., Zhang, H. W. and Wang, X. R. Topological Magnonics: A Paradigm for Spin-Wave Manipulation and Device Design. *Phys. Rev. Appl.* **9**, 024029 (2018).

[42] Gao, W., Lawrence, M., Yang, B., Liu, F., Fang, F., Beri, B., Li, J. and Zhang, S. Topological Photonic Phase in Chiral Hyperbolic Metamaterials. *Phys. Rev. Lett.* **114**, 037402 (2015).

[43] Lapine, M., Shadrivov, I. V. and Kivshar, Y. S. Colloquium: Nonlinear metamaterials. *Rev. Mod. Phys.* **86**, 1093 (2013).

Acknowledgements. – This work was supported by the European Research Council (ERC) (Grant no. ERC-2014-CoG-648328). We acknowledge the use of the UCL Legion High Performance Computing Facility (Legion@UCL) and associated support services in the completion of this work.

Contributions. – N.C.P. conceived the idea and supervised the project. Z.L. and J.W.Y. performed the numerical simulations. Z.L. performed the theoretical analysis. All authors contributed to the preparation of the manuscript.

Competing interests. – The authors declare no competing interests.

Additional information. – Supplementary information for this paper is available online.

METHODS

Chern number calculations. – The Chern number of the n th-band of the photonic crystal is defined by equation (2) [3, 7]. An efficient numerical algorithm to compute it was introduced in Ref. [26]. In this method, from the eigenmode $|\mathbf{E}_n(\mathbf{k})\rangle$ of the n th band, which can be accessed directly from the eigenfrequency solver of COMSOL, one can define a $U(1)$ link variable,

$$U_\alpha(\mathbf{k}_l) = \frac{\langle \mathbf{E}_n(\mathbf{k}_l) | \mathbf{E}_n(\mathbf{k}_l + \mathbf{e}_\alpha) \rangle}{\langle \mathbf{E}_n(\mathbf{k}_l) | \mathbf{E}_n(\mathbf{k}_l + \mathbf{e}_\alpha) \rangle}, \quad (3)$$

where \mathbf{k}_l is a lattice point in the discretized Brillouin zone and \mathbf{e}_α is the lattice displacement in the direction α ($\alpha = 1, 2$). Furthermore, a lattice field strength can be defined by the link variable:

$$F_{12}(\mathbf{k}_l) = \ln \left[U_1(\mathbf{k}_l) U_2(\mathbf{k}_l + \mathbf{e}_1) U_1^{-1}(\mathbf{k}_l + \mathbf{e}_2) U_2^{-1}(\mathbf{k}_l) \right], \quad (4)$$

where the lattice field strength is defined as the principal branch of the logarithm $-\pi < F_{12}(\mathbf{k}_l)/i \leq \pi$. Finally, the Chern number of the n th band can be calculated from the lattice field strength according to:

$$C_n = \frac{1}{2\pi i} \sum_l F_{12}(\mathbf{k}_l), \quad (5)$$

where the sum is taken over all the lattice points in the discretized Brillouin zone. The C_n defined above is manifestly gauge-invariant and strictly an integer for arbitrary lattice parameters. This is because if we introduce a gauge potential

$$A_\alpha(\mathbf{k}_l) = \ln U_\alpha(\mathbf{k}_l), \quad -\pi < A_\alpha(\mathbf{k}_l)/i \leq \pi, \quad (6)$$

one can get

$$F_{12}(\mathbf{k}_l) = \Delta_1 A_2(\mathbf{k}_l) - \Delta_2 A_1(\mathbf{k}_l) + i2\pi n_{12}(\mathbf{k}_l), \quad (7)$$

where $\Delta_\alpha f(\mathbf{k}_l) = f(\mathbf{k}_l + \mathbf{e}_\alpha) - f(\mathbf{k}_l)$ and $n_{12}(\mathbf{k}_l)$ is an integer valued field, chosen in such a way that $F_{12}(\mathbf{k}_l)/i$ takes a value within the principal branch. Consequently, we can get

$$C_n = \sum_l n_{12}(\mathbf{k}_l), \quad (8)$$

which shows that C_n is an integer. Certainly, this does not mean that any coarse discretization of the first Brillouin zone

will ensure a converged Chern number; nevertheless, asymptotic convergence of the Chern number requires only a moderately dense discretization. In our calculations of the data presented in Fig. 2e, we find that a 20×20 discretization of the first Brillouin zone suffices.

Coupled mode theory. – The coupled-mode equations for the second-harmonic generation are (see Supplementary Material):

$$\frac{dA_f(x)}{dx} = i\gamma_f^{(2)}(x)A_f^*(x)A_s(x)e^{i\Delta kx}, \quad (9a)$$

$$\frac{dA_s(x)}{dx} = i\gamma_s^{(2)}(x)A_f^2(x)e^{-i\Delta kx}, \quad (9b)$$

where $A_f(x)$ and $A_s(x)$ are the slowly-varying envelopes of the fundamental and second-harmonic waves, respectively, $\Delta k = k_s(\Omega_2) - 2k_f(\omega_0)$ and the effective second-order nonlinear coefficients $\gamma_f^{(2)}(x)$ and $\gamma_s^{(2)}(x)$ are given by:

$$\gamma_f^{(2)}(x) = \frac{4Z_0^{3/2}\omega_0 n_{g,f} \sqrt{n_{g,s}}}{\sqrt{a}} \chi_{\text{eff},f}^{(2)}(x), \quad (10a)$$

$$\gamma_s^{(2)}(x) = \frac{2Z_0^{3/2}\Omega_2 n_{g,f} \sqrt{n_{g,s}}}{\sqrt{a}} \chi_{\text{eff},s}^{(2)}(x). \quad (10b)$$

Here, Z_0 is the vacuum impedance, $n_{g,f}$ and $n_{g,s}$ are the group indices at the fundamental and second-harmonic frequencies, respectively, and $\chi_{\text{eff},f}^{(2)}(x)$ and $\chi_{\text{eff},s}^{(2)}(x)$ are the effective second-order susceptibilities at the fundamental and second-harmonic frequencies, respectively (see Supplementary Material for their definitions).

Similarly, the coupled-mode equations for the third-harmonic generation are (see Supplementary Material):

$$\frac{dA_f(x)}{dx} = i\gamma_f^{(3)}(x)A_f^{*2}(x)A_t(x)e^{i\Delta kx}, \quad (11a)$$

$$\frac{dA_t(x)}{dx} = i\gamma_t^{(3)}(x)A_f^3(x)e^{-i\Delta kx}, \quad (11b)$$

where $A_f(x)$ and $A_t(x)$ are the slowly-varying envelopes of the fundamental and third-harmonic waves, respectively, $\Delta k = k_t(\Omega_3) - 3k_f(\omega_0)$ and the effective third-order nonlinear coefficients $\gamma_f^{(3)}(x)$ and $\gamma_t^{(3)}(x)$ are given by:

$$\gamma_f^{(3)}(x) = \frac{12Z_0^2\omega_0 n_{g,f} \sqrt{n_{g,f} n_{g,t}}}{a} \chi_{\text{eff},f}^{(3)}(x), \quad (12a)$$

$$\gamma_t^{(3)}(x) = \frac{4Z_0^2\Omega_3 n_{g,f} \sqrt{n_{g,f} n_{g,t}}}{a} \chi_{\text{eff},t}^{(3)}(x), \quad (12b)$$

with $n_{g,t}$ being the group index at the third harmonic.

The above coupled mode equations for SHG and THG are solved and the results, such as, phase-mismatching related oscillations and nonlinear conversion efficiencies, are compared directly with those of the full-wave numerical simulations to validate our main claims.

Numerical simulations. – All numerical simulations presented in this study were performed using COMSOL Multiphysics 5.3, a commercial software package based on the

finite-element method. All computational meshes were set according to the type of “physics-controlled mesh”. The bulk photonic bands presented in Figs. 2c–2e were calculated using the eigenfrequency solver for a single unit cell (see Fig. 2a) with Bloch-periodic boundary conditions imposed at the boundaries of the unit cell. These band structure calculations were validated using Synopsis’s BandSOLVE software. For the edge mode calculations presented in Fig. 3, we considered a PhC strip structure with 30 unit cells along the y -axis and one unit cell along the x -axis, where perfect electric conductor boundary conditions were applied to the top and bottom edges along the y -axis, whereas Bloch-periodic boundary conditions were used for the x -axis. The results for nonlinear mode interactions presented in Figs. 4, 5, and 6 were computed using the “Electromagnetic Waves, Frequency Domain” module.

To simulate the nonlinear frequency mixing processes in COMSOL, we defined two “Electromagnetic Waves, Frequency Domain” models, one for the fundamental frequency ω_0 and one for the second (third) harmonic frequency Ω_2 (Ω_3). The two models are coupled using a “Polarization” feature

added to each of the models. We assumed that for both the SHG and THG cases the nonlinear susceptibilities are diagonal tensors, the diagonal elements being χ_2 and χ_3 , respectively.

For the study of the SHG (where we consider TM-polarized modes), the nonlinear polarizations are:

$$P_{\text{NL},z}^{\omega_0} = 2\chi_2 E_{2z} E_{1z}^*, \quad (13a)$$

$$P_{\text{NL},z}^{\Omega_2} = \chi_2 E_{1z}^2. \quad (13b)$$

For the study of THG, the nonlinear polarizations are:

$$P_{\text{NL},z}^{\omega_0} = 3\chi_3 E_{3z} E_{1z}^{*2}, \quad (14a)$$

$$P_{\text{NL},z}^{\Omega_3} = \chi_3 E_{1z}^3. \quad (14b)$$

The size of the simulation domains and the boundary conditions of Figs. 4, 5, and 6 are given in the corresponding captions.

Data availability. – All data that support the plots and findings reported in this paper are available upon request from the corresponding author.